

ACCRETION DISK RADIATION DYNAMICS AND THE COSMIC BATTERY

LEELA E. KOUTSANTONIOU^{1,2,*} AND IOANNIS CONTOPOULOS^{1,†}

¹ Research Center for Astronomy and Applied Mathematics, Academy of Athens, Athens 11527, Greece

²Department of Astrophysics, Astronomy and Mechanics, Faculty of Physics, University of Athens, Panepistimiopolis Zografos, Athens 15784, Greece

Draft version July 14, 2021

ABSTRACT

We investigate the dynamics of radiation in the surface layers of an optically thick astrophysical accretion disk around a Kerr black hole. The source of the radiation is the surface of the accretion disk itself, and not a central object as in previous studies of the Poynting-Robertson effect. We generate numerical sky maps from photon trajectories that originate on the surface of the disk as seen from the inner edge of the disk at the position of the innermost stable circular orbit (ISCO). We investigate several accretion disk morphologies with a Shakura-Sunyaev surface temperature distribution. Finally, we calculate the electromotive source of the Cosmic Battery mechanism around the inner edge of the accretion disk and obtain characteristic timescales for the generation of astrophysical magnetic fields.

Subject headings: Accretion; Black hole physics; Magnetic fields

notesize

1. INTRODUCTION

From a distance, astrophysical sources of luminosity L look like point sources of isotropic radiation. In that limit, radiation introduces a radial force component per proton

$$f_{\text{rad}}^r = \frac{L\sigma_T}{4\pi r^2 c}, \quad (1)$$

which obviously modifies the dynamics of the surrounding plasma. Here, σ_T is the Thomson cross-section for photon scattering by the plasma electrons, and r is the distance of the orbiting proton. It is important to realize that radiation pressure is felt only by the plasma electrons. As we will show in detail below, the protons feel the radiation force through a radial electric field that develops between them and the electrons.

Eq. (1) is not the only force component in an isotropic radiation field. Matter is in orbit around the center, and therefore, one needs to also take into account the Poynting-Robertson radiation drag. This effect (hereafter PR) was first described in 1903 by J. H. Poynting, but was revisited and fully explained much later in 1937 by H. P. Robertson, with a significant contribution from J. Larmor. Its main application has been in the study of orbits of particles (mainly dust grains) around the Sun. Without radiation drag, the orbits are circular or elliptical. In the presence of radiation, the grains scatter photons emitted by the central star, lose angular momentum, and inspiral toward the star. The question that arises, is how can a force perpendicular to the motion slow down the grain. The answer is obvious when we view the radiation field in the frame of the moving particle. In that frame, the radiation field is aberrated, namely slightly concentrated or beamed in the direction of motion. This aberration results in an extra radiation force opposite to the target's motion that slows it down. In flat spacetime,

the PR azimuthal drag force per proton can be directly calculated as

$$f_{\text{PR}}^\phi = -f_{\text{rad}}^r \frac{v^\phi}{c} = -\frac{L\sigma_T v^\phi}{4\pi r^2 c^2}. \quad (2)$$

Here, v^ϕ is the plasma azimuthal velocity. Another way to view the same effect is through the equivalence of energy and mass, and the conservation of momentum. If we could separate the scattering process into absorption and re-emission of the incoming photon by the target we would see that as the photon is absorbed, the 'mass' of the target increases, and therefore its speed decreases. During the re-emission, however, the outgoing photon carries away mass as well as momentum, leaving the target's speed unchanged. In total, every time the target 'absorbs' a photon, it slows down and falls into a lower orbit. This is the reason why the PR effect is called a drag or braking. As before, the protons in a plasma feel the PR drag through an azimuthal electric field that develops between them and the electrons.

The astrophysical setting of an accreting rotating black hole is far more complex, and the dynamics of its radiation field have not been thoroughly investigated before. In Kerr spacetime, photon orbits are curved and there are several shifts that change the photon frequency during its travel through the curved and inhomogeneous spacetime. The fact that now the source of radiation is also rotating, further complicates the problem by introducing an extra Doppler shift. If the central object is not a black hole but a slowly rotating compact spherical star, then simplifications can be made to the problem, making the process of solution somewhat easier. This case was studied by Abramowicz, Ellis & Lanza (1990), and in a series of papers by Miller and Lamb (Miller & Lamb 1993; Lamb & Miller 1995; Miller & Lamb 1996). Bini *et al.* (2008) & (2011) studied the PR effect for photons and test particles in the equatorial plane. The background spacetime was taken to be Schwarzschild and Kerr. Oh *et al.* (2010) further studied 'suspension orbits' around a slowly rotating compact star with an isotropic radiation field. In

* leelamk@phys.uoa.gr

† icontop@academyofathens.gr

all previous works, a simple radiation field was assumed (one emanating from a central spherical object). On the other hand, astrophysical sources associated with accretion disks are expected to generate a complex radiation field with ensuing complex dynamics in the vicinity of the central object.

We were, therefore, compelled to develop a fully relativistic ray tracing code that calculates the radiation field and takes into account the spatial extent and rotation of its source. Our primary interest is to study the dynamical effect of radiation around rapidly rotating black holes, where extremely energetic photons and strong magnetic fields are expected to be present. As material is pulled from its surroundings (companion star, stellar wind, interstellar medium, etc.) it forms a rotating disk around the center. This material slowly loses angular momentum through a number of different mechanisms of varying efficiency (magnetorotational instability-MRI, magnetic braking by disk winds/jets, PR drag, viscosity, turbulence, tidal forces, gravitational waves, etc.) and inspirals towards the center. As it accretes, the temperature rises to values of the order of 10^7 K or even higher. At these temperatures, matter radiates in the X-ray part of the spectrum, giving us what we observe and know as an X-ray binary (in the case of a stellar mass black hole), or an AGN (in the case of a supermassive black hole). Since at this point the disk speed is a considerable fraction of the speed of light and the radiation luminosity a considerable fraction of its Eddington value, we expect that the dynamical effects of radiation will not only be noticeable but in some cases they may even be dominant.

In the present paper, we calculate the radiation pressure at the position of the Innermost Stable Circular Orbit (hereafter ISCO) around a rotating Kerr black hole. Our work is original in that

- (a) the source of radiation is the surface of the accretion disk around the black hole which radiates as a black body of various temperatures, and
- (b) we consider the effect on the whole plasma and not on individual particles like dust grains (as in the original discussion of the PR drag effect).

In § 2 we formulate the problem in general relativity and describe our course of action toward its solution. In § 3 we present our problem setup and numerical results. In § 4 we discuss the effect of radiation pressure in generating astrophysical magnetic fields through the mechanism of the Cosmic Battery. Finally, in § 5 we present our conclusions and discuss prospects for future work.

notesize

2. MATHEMATICAL FORMULATION

We will assume that the immediate environment of an accreting rotating black hole can be described by the Kerr spacetime metric. We will follow closely the train of thought and logic of ? correcting minor mistakes along the way. We will hereafter use geometrical units in which $c = G = 1$. Latin/Greek indices will denote space/spacetime components respectively. We will also assume the Einstein notation for summation over double indices.

2.1. The Kerr metric

A Kerr black hole is characterized by its mass M and its angular momentum J , or equivalently its spin parameter $a \equiv J/M$. a takes values between zero (for a non-rotating Schwarzschild black hole) and M (for a maximally rotating black hole). Physical quantities are measured by Zero Angular Momentum Observers (ZAMOs; also known as local Fiducial Observers or Fidlos) in their Locally Non-Rotating Frame (LNRF). In Boyer-Lindquist (t, r, θ, ϕ) coordinates, the Kerr metric reads

$$ds^2 = -\alpha^2 dt^2 + \varpi^2 (d\phi - \omega dt)^2 + \frac{\Sigma}{\Delta} dr^2 + \Sigma d\theta^2, \quad (3)$$

where,

$$\alpha = (\Delta \Sigma / A)^{1/2},$$

$$\omega = 2aMr/A,$$

$$\varpi = (A/\Sigma)^{1/2} \sin \theta.$$

$$\Sigma = r^2 + a^2 \cos^2 \theta,$$

$$\Delta = r^2 - 2Mr + a^2,$$

$$A = (r^2 + a^2)^2 - a^2 \Delta \sin^2 \theta$$

Here, α is the lapse function, ω is the angular velocity of ZAMOs, and ϖ is the cylindrical radius. It is possible to transform four-vectors p^μ from the Boyer-Lindquist coordinates to $p^{\hat{\mu}}$ in the LNRF and back via the relations

$$p^\mu = e_\nu^\mu p^{\hat{\nu}} \quad \text{and} \quad p^{\hat{\mu}} = e_\nu^{\hat{\mu}} p^\nu, \quad (4)$$

where the transformation tensor components are given explicitly as

$$e_t^t = \alpha^{-1}, \quad e_t^\phi = \omega \alpha^{-1},$$

$$e_r^r = \left(\frac{\Sigma}{\Delta} \right)^{-1/2}, \quad e_\theta^\theta = \Sigma^{-1/2}, \quad e_\phi^\phi = \varpi^{-1}, \quad (5)$$

$$e_t^{\hat{t}} = \alpha, \quad e_t^{\hat{\phi}} = -\omega \varpi,$$

$$e_r^{\hat{r}} = \left(\frac{\Sigma}{\Delta} \right)^{1/2}, \quad e_\theta^{\hat{\theta}} = \Sigma^{1/2}, \quad e_\phi^{\hat{\phi}} = \varpi. \quad (6)$$

We have introduced here the notation that unhatted indices refer to the Boyer-Lindquist frame whereas hatted ones to the LNRF.

We remind the reader that there are two characteristic surfaces around a Kerr black hole. The first surface, the black hole event horizon, corresponds to the outer root of the equation $\Delta = 0$, at $r_{\text{BH}} = M + \sqrt{M^2 - a^2}$. This is a sphere with radius $r_{\text{BH}} = 2M$ for a non-rotating (Schwarzschild) black hole and radius M for a maximally rotating one. The event horizon is a one-way membrane in the sense that particles, massive or massless, that follow timelike or null geodesics respectively, can only cross this surface in one direction: inwards. The second surface, the static limit, corresponds to the surface inside which the metric time component $g_{tt} \equiv \omega^2 \varpi^2 - \alpha^2$ becomes positive. The static limit and the event horizon are always in contact at the rotation axis and differ the

most on the equatorial plane, where the static limit extends out to a radial distance of $2M$ for all spin parameters. The region between the horizon and the static limit is called the ergosphere. Another characteristic radius is the position of the ISCO, r_{ISCO} , on the equator. It is generally assumed that the inner edge of the accretion disk around the black hole coincides with the ISCO, although this may vary considerably around exceedingly bright or strongly magnetized sources (Balbus 2012, Contopoulos & Papadopoulos 2013). For prograde rotation, r_{ISCO} ranges from $6M$ for a Schwarzschild black hole, to M for a maximally rotating one¹.

2.2. The radiation force

The radiation field in the deep interior of an optically thick astrophysical disk is thermal. In the present paper, though, we are mainly interested in the dynamics of radiation in the surface layers which ‘see’ photons coming from the whole surface of the disk. The radiation force per proton, f_{rad}^i , is a non-gravitational term that enters the relativistic equation of motion for the spatial velocity components as

$$\frac{d^2 u^i}{d\tau^2} + \Gamma_{\nu\kappa}^i u^\nu u^\kappa = \frac{f_{\text{rad}}^i}{m_p}. \quad (7)$$

Here, u^μ is the plasma four-velocity, τ is the plasma proper time, $\Gamma_{\nu\kappa}^\mu$ are the metric Christoffel symbols, and m_p is the proton mass. We have assumed for simplicity that the innermost accretion disk plasma consists of protons and electrons. We have also assumed that electromagnetic and gas pressure forces are negligible. The ϕ -component of the radiation force f_{rad}^ϕ is the generalization of the PR drag per proton.

A short comment on eq. (7) is in order here. The radiation force is felt only by the plasma electrons (the Thomson cross-section for the protons is roughly four million times smaller than that for the electrons), yet the full plasma feels the radiation force. This becomes clear when we consider the equations of motion for the plasma electrons and protons independently, namely

$$m_e \frac{d^2 u_e^i}{d\tau^2} + m_e \Gamma_{\nu\kappa}^i u_e^\nu u_e^\kappa = f_{\text{rad}}^i - eE^i \quad \text{and} \quad (8)$$

$$m_p \frac{d^2 u_p^i}{d\tau^2} + m_p \Gamma_{\nu\kappa}^i u_p^\nu u_p^\kappa = eE^i, \quad (9)$$

where the electron charge is equal to $-e$, and E^i is called the ‘impressed’ electromotive field that summarizes the effect of the various non-electrical non-gravitational forces in the induction equation (see below; Biermann & Schluter 1951). Since, $m_e \ll m_p$, one can ignore the m_e -terms in eq. (8) and obtain

$$E^i \approx \frac{f_{\text{rad}}^i}{e}. \quad (10)$$

Putting this back in eq. (9) we obtain

$$\frac{d^2 u_p^i}{d\tau^2} + \Gamma_{\nu\kappa}^i u_p^\nu u_p^\kappa \approx \frac{f_{\text{rad}}^i}{m_p}, \quad (11)$$

¹ We note that even though it seems like the horizon, the ISCO and other surfaces coincide at $r = M$ for a maximally rotating BH ($a = M$), they differ in proper radial distances. This illusion is the result of a coordinate singularity in the Boyer-Lindquist frame.

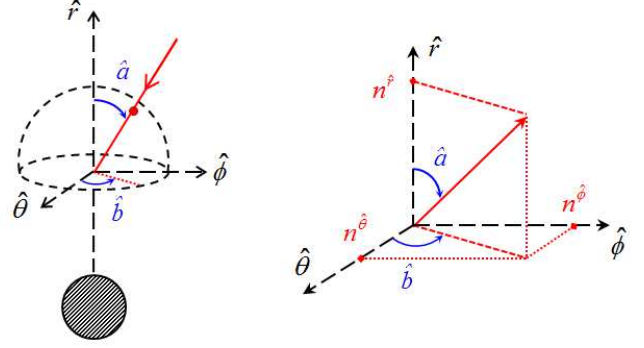


Figure 1. The local sky around the target particle. For the direction of the incoming photon, we define angles \hat{a} and \hat{b} similar to the polar angle θ and the azimuthal angle ϕ of the typical spherical coordinates. The striped disk represents the event horizon of the central black hole.

which is just eq. (7) under the approximation that $u_p^\mu \approx u^\mu$. In other words, *the protons feel the radiation force through the electric field that develops between them and the electrons*. In § 4 we will come back to this important effect which has been discussed since the late 1940s, but is often ignored by the younger generation of researchers. f_{rad}^i is connected to the radiation flux F^i through the formula

$$f_{\text{rad}}^i = \sigma_T F^i. \quad (12)$$

We have assumed for simplicity that the Thomson cross-section σ_T is independent of the radiation frequency and scattering angle². The radiation flux components F^i are given by

$$F^i = h_\nu^i T^{\kappa\nu} u_\kappa, \quad (13)$$

where $T^{\kappa\nu}$ is the radiation stress-energy tensor, and h_ν^μ is a tensor that projects orthogonally to the target four-velocity and is given by

$$h_\nu^\mu = -\delta_\nu^\mu - u^\mu u_\nu. \quad (14)$$

From the above, we see that in order to calculate the radiation force, we need to calculate its stress-energy tensor $T^{\kappa\nu}$ in Boyer-Lindquist coordinates, or equivalently $T^{\hat{\kappa}\hat{\nu}}$ in the LNRF. The two are connected through the transformation

$$T^{\mu\nu} = e_{\hat{\kappa}}^\mu e_{\hat{\lambda}}^\nu T^{\hat{\kappa}\hat{\lambda}}. \quad (15)$$

2.3. The radiation stress-energy tensor

In the LNRF, the radiation stress-energy tensor is given by

$$\begin{aligned} T^{\hat{\mu}\hat{\nu}} &= \iint I_\nu(r, \theta, \hat{a}, \hat{b}; \nu) d\nu n^{\hat{\mu}} n^{\hat{\nu}} d\Omega, \\ &= \int I(r, \theta, \hat{a}, \hat{b}) n^{\hat{\mu}} n^{\hat{\nu}} d\Omega, \end{aligned} \quad (16)$$

where, I_ν and I are the frequency dependent and integrated specific intensities respectively in the LNRF at

² For an incoming photon of energy 1 keV, the cross section deviation from the uniform case of σ_T is in total very small and at most equal to $\sigma_T/2$. Therefore we choose to ignore it in the present work, in order to avoid the notably more complex calculations required in this case.

the position of the target electron. Here, $n^{\hat{i}} \equiv p^{\hat{i}}/p^{\hat{t}}$ is the unit spacelike vector along the photon trajectory that hits the target, and $p^{\hat{\mu}}$ are the photon four-momentum components in the LNRF. We define angles \hat{a} , \hat{b} as shown in Figure 1 and therefore we have

$$n^{\hat{r}} = \cos \hat{a}, \quad n^{\hat{\theta}} = \sin \hat{a} \cos \hat{b}, \quad n^{\hat{\phi}} = \sin \hat{a} \sin \hat{b}. \quad (17)$$

Radiation photons originate on the surface of the accretion disk, travel to the position of the target, and reach it from a certain direction $n^{\hat{i}}$ that corresponds to a solid angle element $d\Omega = \sin \hat{a} d\hat{a} d\hat{b}$. In other words, the integral in eq. (16) has contributions *only* from those directions that correspond to photon trajectories that originate on the radiation source, in our case the surface of the hot innermost accretion disk. Therefore, the calculation of the radiation field requires the *backward integration* of photon trajectories from the position of the target to their origin on the surface of the disk along all directions (\hat{a}, \hat{b}) in the sky of the target particle.

For each such photon trajectory, the specific intensity I_{ν} that appears in eq. (16) is *different* from the source specific intensity $I_{\nu,s}$. In order to obtain I_{ν} we take advantage of the fact that, along the path of a light ray, $I_{\nu}/\nu^3 = I_{\nu,s}/\nu_s^3$ for the frequency dependent specific intensity, or equivalently

$$I = \left(\frac{\nu}{\nu_s} \right)^4 I_s \quad (18)$$

for the frequency integrated intensities, where the subscript s refers to quantities calculated at the radius of the source. Notice that the ratio ν/ν_s expresses a frequency shift that is *independent* of the frequency itself and depends only on the form of the spacetime and the angle of emission. It accounts for three different phenomena: the gravitational redshift caused by gravitational time dilation, the Doppler shift caused by the motion of the emitting surface, and the frame dragging shift caused by the ‘differential rotation’ of the spacetime. The former two shifts can be encountered in any spacetime, while the latter only in rotating spacetimes.

The gravitational redshift between an emitted frequency ν' and a received frequency ν is given by

$$\frac{\nu}{\nu'} = \frac{\alpha'}{\alpha}, \quad (19)$$

which is, as expected, equal to the inverse ratio of the elements of proper time in each point of the spacetime³. The Doppler shift can be calculated by the familiar formula

$$\frac{\nu}{\nu'} = \frac{1}{\gamma(1 - v \cos \psi)}, \quad (20)$$

where $\gamma = (1 - v^2)^{-1/2}$ is the Lorentz factor and ψ is the angle between the direction of motion of the emitting surface and the direction of the photon emission. Both γ and ψ are measured in the LNRF at the point of emission

³ Notice that eq. (19) involves the lapse functions α , whereas the equivalent expression in Miller & Lamb 1996 involves the metric time elements g_{tt} .

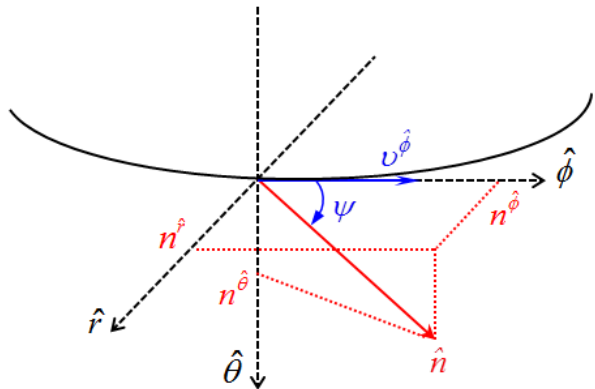


Figure 2. The photon emission along the direction \hat{n} and the disk motion with velocity $v \equiv v^{\hat{\phi}}$ at the point of emission. The arc represents a part of the circular orbit of the disk element that emitted the photon.

(Figure 2). Finally, the frame dragging shift is equal to

$$\frac{\nu}{\nu'} = \frac{1 + \omega \frac{p_{\phi}}{p_t}}{1 + \omega' \frac{p_{\phi}}{p_t}}, \quad (21)$$

where p_{μ} are the emitted photon covariant four-momentum components. Notice that the ratio p_{ϕ}/p_t depends on the direction of emission of each such photon at its origin (see § 3 below), and is conserved along the photon trajectory.

In our present study we consider all three of the above shifts between the frequency ν_s of the emitted photons at their source as seen by an observer comoving with the source, and the frequency ν observed in the LNRF at the position of the target. The Doppler shift of eq. (20) takes us from the frame comoving with the source of photons to the LNRF at that position. Subsequently, the frame dragging shift of eq. (21) takes us from the LNRF rotating with ω_s at the position of the source to the LNRF rotating with ω at the position of the target. In the meantime, the gravitational redshift of eq. (19) accounts for the difference in time dilation between these two points (see Figure 3). Thus, combining eqs. (19), (20) and (21), we deduce the total shift between the emitted and received frequencies ν_s and ν

$$\frac{\nu}{\nu_s} = \frac{\alpha_s}{\alpha} \frac{1 + \omega \frac{p_{\phi}}{p_t}}{1 + \omega_s \frac{p_{\phi}}{p_t}} \frac{1}{\gamma(1 - v^{\hat{\phi}} \cos \psi)}. \quad (22)$$

From eqs.(18) and (22), the specific intensity we seek is simply given by

$$I = \frac{\alpha_s^4}{\alpha^4} \left(\frac{1 + \omega \frac{p_{\phi}}{p_t}}{1 + \omega_s \frac{p_{\phi}}{p_t}} \right)^4 \frac{I_s}{\gamma^4 (1 - v^{\hat{\phi}} \cos \psi)^4} \quad (23)$$

along each photon trajectory.

notsize

3. NUMERICAL SIMULATIONS

As explained at the end of the previous Section, the complex astrophysical setup that we are considering (ac-

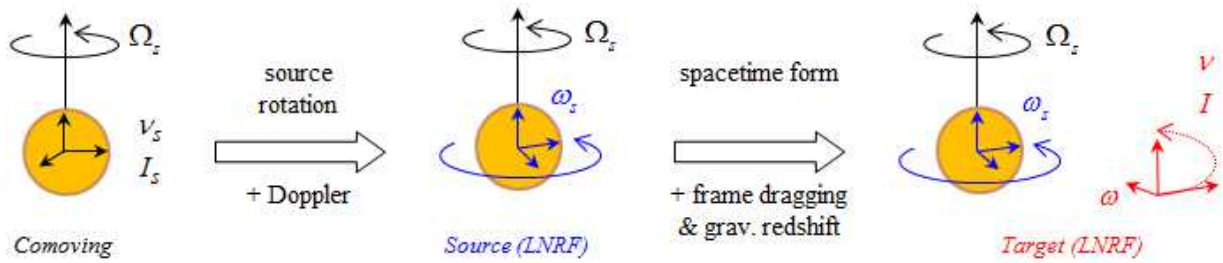


Figure 3. Visual representation of the frame change process. When we are comoving with the source we measure a specific intensity I_s . In order to measure it at the LNRF at the source, we must account for the Doppler shift due to the rotation. To calculate the specific intensity I observed at the target electron, we must take into account the spacetime curvature effects, namely the gravitational redshift due to time dilation and the frame dragging shift due to the 'differential rotation' of the spacetime at different radii. The yellow orb is a sphere with the radius of the emitting surface, whatever that might be (a part of the accretion disk, the surface of a star, etc) and not the black hole event horizon.

cretion disk + rotating black hole) requires backward ray tracing along every direction (\hat{a}, \hat{b}) in the sky of the target. In this present work, we only consider an optically thick accretion disk. In particular, we only consider target electrons located in a thin surface layer at the inner edge of the disk at the position of the ISCO on the equator. The photon trajectories that we obtain are divided into three categories, depending on their point of origin: those that cross the event horizon, those that originate from a point at ‘infinity’ or the ‘outer disk’ (we arbitrarily take $r > 12GM/c^2$) and those that originate from a point of the inner disk ($r_{\text{ISCO}} \leq r \leq 12GM/c^2$). Trajectories from the first two categories do not give any significant contribution to the radiation field. Radiation pressure is due to photons of the third category that originate from the innermost hotter part of the disk. For those ‘allowed photon trajectories’ we calculate their point of origin, their direction of emission, and the resulting frequency shifts between the emission and destination points. For those photons we will assume that the surface of the disk radiates as a black body with temperature T that varies as a known function of distance r_s on the disk (e.g. $T \propto r_s^{-3/4}$ as in Shakura & Sunyaev 1976). In that case, the expression that enters eq. (23) becomes

$$I_s = \frac{\sigma_B}{\pi} T^4(r_s) \quad (24)$$

where σ_B is the Stefan-Boltzmann constant (Rybicki & Lightman 1986).

In order to implement the above numerical procedure, we developed two numerical codes:

1. Code *Omega* for the ray tracing, and
2. Code *Infinity* that calculates the energy-momentum tensor through the integral in eq. (16) and the radiation force through eq. (12)

Code *Omega* calculates single photon trajectories for given angles (\hat{a}, \hat{b}) of the incoming photon, finds out whether the trajectory originates from the inner hotter part of the disk between r_{ISCO} and $12GM/c^2$ (the outer boundary is defined arbitrarily for computational convenience), and if yes, returns its point and angles of origin. All problem parameters can be easily input by the user. Code *Infinity* divides the sky at the ISCO into half a degree intervals in both \hat{a} and \hat{b} , and runs code *Omega* for every angle. This corresponds to roughly 260.000 photon trajectories per run. It finds the allowed trajectories, calculates the frequency shifts for each angle, and generates the radiation matrix. From that, the radiation stress-energy tensor and the four-force components are computed. We tested our code in the Schwarzschild case with a central source of radiation and obtained agreement with the analytic formulae given by Abramowicz, Ellis & Lanza (1990) to within 0.7% on average.

In Figure 4, we present sky maps, namely the sky as seen in the LNRF at the position of the moving target particle at the ISCO, for various values of the black hole spin parameter. We have assumed here that the disk is in Keplerian prograde rotation around the central black hole. We have also assumed that it is optically thick. Our calculations were performed

with a Shakura-Sunyaev disk surface temperature profile $T(r_s) = 10^7 \text{ K } (r_s/r_{\text{ISCO}})^{-3/4}$. In each frame, the center of the black hole ($\hat{a} = \pi$) is at the center, and the direction perpendicular to that ($\hat{a} = \pi/2$) is on the circumference. The circle of radiation around the black hole horizon that appears in most of the images is an Einstein ring generated from the disk upper and lower surfaces. Notice the difference in the radiation intensity from left to right due to the material on the right moving toward the target, and the material on the left moving away from it. Column (a) corresponds to an infinitesimally thin disk. In this special case, radiation hits the target even from directions away from the black hole that correspond to $0 \leq \hat{a} < \pi/2$. These directions are not shown in Figure 4, but are taken into account in the calculation of the integral in eq. (16). Column (b) corresponds to a model for a thin disk with height equal to $0.1M$. Column (c) corresponds to a model for a thick disk with height equal to $0.5M$. Finally, column (d) corresponds to a thick torus with circular cross-section that extends from $r = r_{\text{ISCO}}$ to $r = 3r_{\text{ISCO}}$ along the equator. For a better understanding of the rotating spacetime effects on the photon trajectories, the reader is referred to Appendix B and Figure 5 where we show how the morphology of photon trajectories changes with impact angle and black hole spin.

In Tables 1 and 2, we present our numerical results for the r - and ϕ -components of the radiation force per proton respectively (normalized to the canonical gravitational force per proton GMm_p/r_{ISCO}^2) for various black hole spin parameters and for various accretion disk geometries. As we said before, we have assumed here for simplicity that the accretion disk is in Keplerian prograde rotation (Bardeen *et al.* 1972) with $v^{\hat{r}} \ll v^{\hat{\phi}}$ (see Appendix A). More realistic accretion disk configurations will be considered in a future work. What we found is most interesting and rather unexpected:

1. In the theoretical case of an infinitely thin disk, radiation hits the electrons at the ISCO from all directions. It is thus expected that the radiation field is almost isotropic, and therefore, the aberration due to the orbital motion of the target electrons at the ISCO results in radiation drag. This is the general relativistic generalization of the PR drag for thin astrophysical accretion disks. A similar effect is expected to take place when the accretion disk is geometrically thick but optically thin, as is the case of an ADAF disk (Narayan & Yi 1994).
2. As the inner edge of the disk thickens, photons can reach the ISCO electrons only from the half space facing the black hole (we have assumed zero optical depth in the disk interior). The important new element is that the radiation that originates on the ISCO contributes more and more to the total radiation pressure, and the radiation field is distorted by the disk and spacetime rotations. As a result, the radiation force acts *along the direction of rotation*, and the azimuthal force component changes sign from negative to positive. In other words, *the azimuthal effect of radiation changes from drag to acceleration*. Considering the analogy with the classical Poynting-Robertson effect, this result was

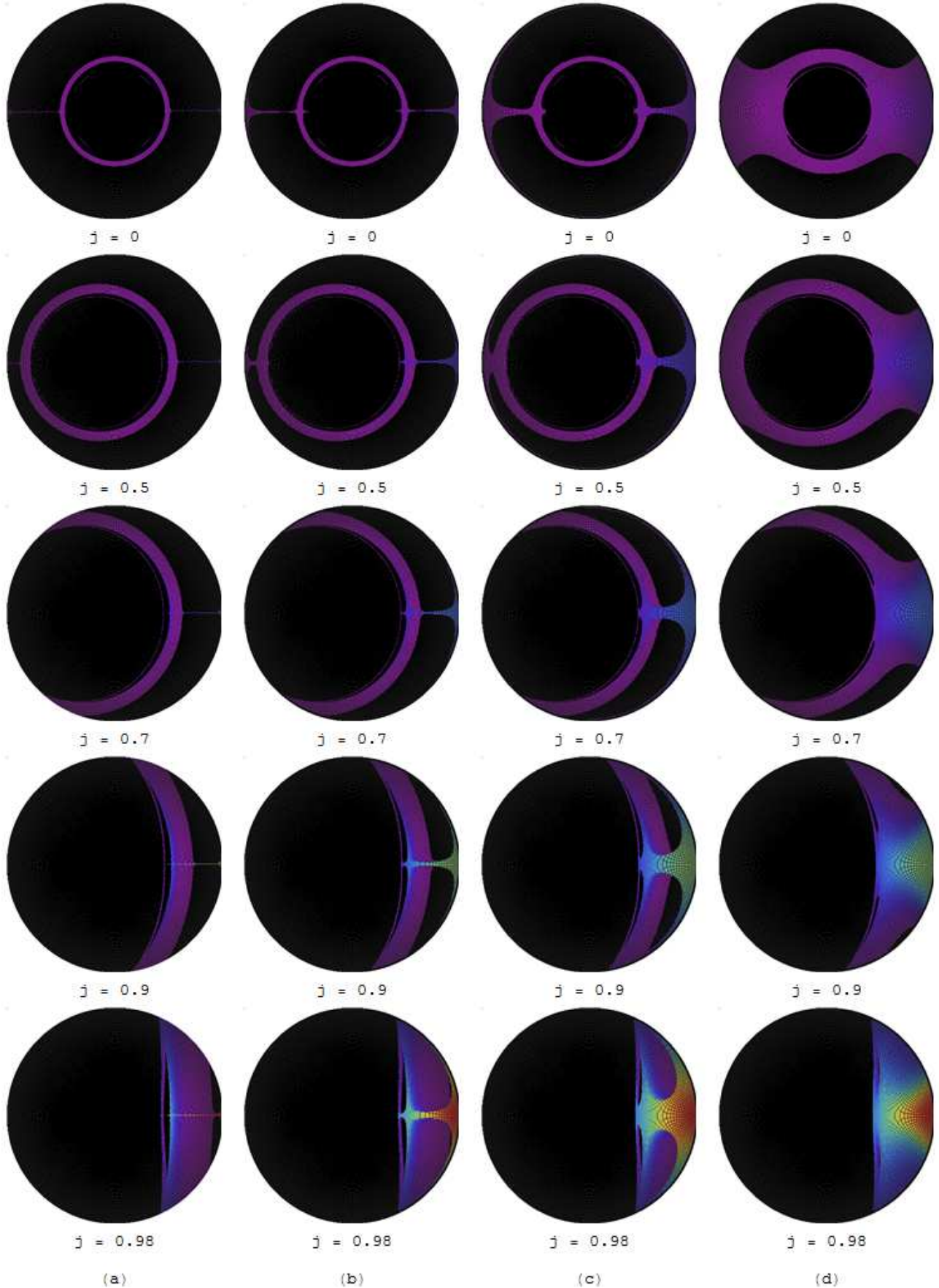


Figure 4. The sky as seen in the LNRf at the position of the moving target particle at the ISCO, for various values of the black hole dimensionless spin parameter $j \equiv a/M$. The color scale corresponds to $I(\hat{a}, \hat{b})$ at the ISCO. In each frame, the center of the black hole is at the center ($\hat{a} = \pi$), and the direction perpendicular to that ($\hat{a} = \pi/2$) is on the circumference. Column (a): infinitesimally thin disk; column (b): thin disk; column (c): thick disk; column (d): thick torus (see text for details). The black hole horizon is the distorted black circle. The circle of radiation around the black hole horizon is the Einstein ring from the upper and lower surfaces of the disk. Notice the difference in radiation intensity from left to right due to the disk and spacetime rotations. We only considered here prograde Keplerian accretion disks and a Shakura-Sunyaev surface temperature profile.

Table 1
Normalized radial radiation force $f_{\text{rad}}^r / \frac{GMm_p}{r_{\text{ISCO}}^2}$

j=a/M	$r_{\text{ISCO}}(\text{M})$	Inf. disk	Thin disk	Thick disk	Torus
0	6.000	0.017	0.021	0.038	0.140
0.1	5.669	0.018	0.022	0.040	0.136
0.2	5.329	0.018	0.023	0.041	0.132
0.3	4.979	0.018	0.023	0.042	0.128
0.4	4.614	0.018	0.024	0.044	0.124
0.5	4.233	0.018	0.024	0.046	0.120
0.6	3.829	0.018	0.024	0.047	0.115
0.7	3.393	0.016	0.024	0.049	0.109
0.8	2.907	0.013	0.025	0.052	0.102
0.9	2.321	0.004	0.025	0.055	0.090
0.92	2.180	0.001	0.025	0.056	0.085
0.94	2.024	-0.004	0.025	0.056	0.080
0.96	1.843	-0.013	0.025	0.055	0.073
0.98	1.614	-0.030	0.024	0.052	0.061

Note. — Numerical results for the r -component of the radiation force per proton f_{rad}^r , normalized to the canonical gravitational force per proton GMm_p/r_{ISCO}^2 for various black hole spin parameters and accretion disk geometries. We assumed Keplerian prograde disk rotation for simplicity, and a Shakura-Sunyaev disk surface temperature profile $T(r_s) = 10^7 \text{ K } (r_s/r_{\text{ISCO}})^{-3/4}$.

Table 2
Normalized azimuthal radiation force $f_{\text{rad}}^\phi / \frac{GMm_p}{r_{\text{ISCO}}^2}$

j=a/M	$r_{\text{ISCO}}(\text{M})$	Inf. disk	Thin disk	Thick disk	Torus
0	6.000	-0.007	0.003	0.037	0.111
0.1	5.669	-0.008	0.003	0.041	0.122
0.2	5.329	-0.010	0.004	0.047	0.135
0.3	4.979	-0.012	0.004	0.054	0.153
0.4	4.614	-0.014	0.005	0.066	0.178
0.5	4.233	-0.016	0.008	0.083	0.214
0.6	3.829	-0.019	0.017	0.117	0.275
0.7	3.393	-0.020	0.053	0.194	0.382
0.8	2.907	-0.019	0.115	0.344	0.589
0.9	2.321	0.002	0.307	0.833	1.187
0.92	2.180	0.016	0.405	1.075	1.459
0.94	2.024	0.040	0.567	1.464	1.870
0.96	1.843	0.092	0.863	2.179	2.576
0.98	1.614	0.242	1.638	3.979	4.171

Note. — Same as Table 1 for the ϕ -component of the radiation force per proton f_{rad}^ϕ .

rather unexpected.

We will next discuss one interesting consequence of our results, namely the role of the azimuthal radiation drag or acceleration in the generation of astrophysical magnetic fields.

notesize

4. THE COSMIC BATTERY

Before we proceed, a short introduction on the Cosmic Battery is in order here. Energetic astrophysical jets have always been associated with relatively strong large scale magnetic fields that extract energy from the

rotation of a central black hole and its surrounding accretion disk (Lovelace 1976, Blanford 1976). This natural association, however, does not answer the fundamental question of what is the origin of the large scale magnetic field.

Magnetic fields are naturally generated in the disk deep optically thick interior through a battery mechanism which focuses mainly on the misalignment between the directions of thermal pressure and density gradients (Biermann 1950). These fields are subsequently amplified through dynamo mechanisms based on various rotational and convective disk instabilities. Unfortunately, when one considers the back-reaction of the field on the dynamics of the disk plasma, dynamo action seems to be very inefficient, and as the field at small diffusive scales reaches equipartition, its large-scale component remains several orders of magnitude weaker than the large scale magnetic field expected at the origin of astrophysical jets (Vainshtein & Cattaneo 1992, Zrake & MacFadyen 2012).

When the disk is non-diffusive, standard MHD advection can bring the field in from large distances and thus naturally account for the origin of the large scale magnetic field in the innermost region of the accretion disk (as attested by the multitude of ideal MHD simulations of magnetized astrophysical accretion disks). When this is not the case, i.e. when the magnetic Prandtl number -the ratio of flow kinematic viscosity to magnetic diffusivity- in a real astrophysical disk is smaller than some critical value of order unity (see Contopoulos & Kazanas 1998 for details), the Cosmic Battery provides one possible solution to the same problem. This is a different battery mechanism that focuses on the anisotropic radiation pressure in the surface layers of the disk which, as we will see, naturally generates the large scale dipolar magnetic field expected at the origin of astrophysical jets.

Eq. (10) yields the plasma electric field as measured in Boyer-Lyndquist coordinates. A similar result applies in the LNRF, namely

$$E^{\hat{i}} = \frac{f_{\text{rad}}^{\hat{i}}}{e}, \quad (25)$$

$$f_{\text{rad}}^{\hat{i}} = \sigma_T F^{\hat{i}} \text{ and } F^{\hat{i}} = h_{\hat{\nu}}^{\hat{i}} T^{\hat{\kappa}\hat{\nu}} u_{\hat{\kappa}}, \quad (26)$$

where, $h_{\hat{\nu}}^{\hat{\mu}} = -\delta_{\hat{\nu}}^{\hat{\mu}} - u^{\hat{\mu}} u_{\hat{\nu}}$ and $u^{\hat{\mu}} = e_{\hat{\nu}}^{\hat{\mu}} u^{\nu}$. In Table 3 we present our numerical results for the $\hat{\phi}$ -component of the electromotive force per proton calculated in the LNRF (once again normalized to the canonical gravitational force per proton GMm_p/r_{ISCO}^2) for various black hole spin parameters and accretion disk geometries. Knowledge of the electric field as seen by ZAMOs in the LNRF allows us to obtain the rate of change with global time t of the total poloidal (meridional) magnetic flux Ψ_{ISCO} accumulated inside the ISCO, namely

$$\frac{\partial \Psi_{\text{ISCO}}}{\partial t} = 2\pi\alpha\varpi_{\text{ISCO}} \left([\mathbf{v} \times \mathbf{B}]^{\hat{\phi}} - \frac{f_{\text{rad}}^{\hat{\phi}}}{e} + \eta[\nabla \times \mathbf{B}]^{\hat{\phi}} \right), \quad (27)$$

where

$$\Psi_{\text{ISCO}} \equiv \pi\mathcal{B}\varpi_{\text{ISCO}r_{\text{ISCO}}} \quad (28)$$

(eq. 2.20d Macdonald & Thorne 1982). Here, $\mathbf{v}^{\hat{i}} \equiv u^{\hat{i}}/u^{\hat{t}}$,

Table 3Normalized azimuthal radiation force $f_{\text{rad}}^{\hat{\phi}}/ \frac{GMm_{\text{p}}}{r_{\text{ISCO}}^2}$ in the LNRF

j=a/M	$r_{\text{ISCO}}(\text{M})$	Inf. disk	Thin disk	Thick disk	Torus
0	6.000	-0.007	0.003	0.037	0.111
0.1	5.669	-0.008	0.003	0.040	0.118
0.2	5.329	-0.010	0.003	0.043	0.126
0.3	4.979	-0.012	0.002	0.047	0.134
0.4	4.614	-0.015	0.001	0.052	0.145
0.5	4.233	-0.018	0.001	0.059	0.157
0.6	3.829	-0.023	0.002	0.071	0.175
0.7	3.393	-0.028	0.021	0.098	0.198
0.8	2.907	-0.039	0.036	0.124	0.214
0.9	2.321	-0.061	0.054	0.163	0.230
0.92	2.180	-0.070	0.060	0.174	0.232
0.94	2.024	-0.084	0.067	0.187	0.235
0.96	1.843	-0.106	0.075	0.203	0.236
0.98	1.614	-0.158	0.089	0.227	0.233

Note. — Same as Table 1 for the $\hat{\phi}$ -component of the radiation force per proton $f_{\text{rad}}^{\hat{\phi}}$ in the LNRF. This is the Cosmic Battery source term in the induction equation expressed in that frame.

\mathcal{B} is some average value of the axial magnetic field threading the region inside the inner edge of the accretion disk, and η is the effective disk magnetic diffusivity. We repeat once again that, in order to focus on the effect of the Cosmic Battery in the surface layers, we have ignored here for simplicity other non-electric non-gravitational forces that may be important in other parts of the accretion disk.

The second term in the r.h.s. of eq. (27) generates an axial magnetic field which may be along the direction of the angular velocity vector in the disk if $f_{\text{rad}}^{\hat{\phi}}$ is negative (i.e. if radiation results in an azimuthal drag force in the LNRF at the inner edge of the disk), or opposite to that if $f_{\text{rad}}^{\hat{\phi}}$ is positive (i.e. if radiation results in an accelerating azimuthal force in the LNRF at the inner edge of the disk). The magnetic flux that builds up obviously closes further out through the accretion disk where $f_{\text{rad}}^{\hat{\phi}}$ drops to zero. The axial magnetic field will be carried by the accretion flow (first term in the r.h.s. of eq. 27), assuming ideal MHD conditions around and inside the ISCO, and the flux accumulated inside the inner edge of the disk will keep growing. The growth will cease, and the mechanism will saturate if the flow begins to also carry inward the return polarity of the magnetic field (Contopoulos & Kazanas 1998, Bisnovatyi-Kogan *et al.* 2002). Nevertheless, the return polarity lies in a region where magnetic diffusivity is significant and the third term in the r.h.s. of eq. (27) dominates over the first one (van Ballegoijen 1989; Lubow *et al.* 1994; Lovelace *et al.* 1994; see also, however, Lovelace *et al.* 2009). Therefore, the return magnetic field *diffuses outward through the disk*, and the mechanism does not saturate but increases the magnetic field to equipartition values⁴. This natural scenario where the innermost part of the accretion disk generates and holds one polarity of the magnetic field, while the return polarity diffuses outward through the outer diffu-

⁴ This point was missed by Bisnovatyi-Kogan *et al.* (2002).

Table 4Cosmic Battery timescales $t_{\text{CB}} = \frac{e\mathcal{B}_o r_{\text{ISCO}}}{\alpha_{\text{ISCO}} f_{\text{rad}}^{\hat{\phi}} c}$ (in hours)

j=a/M	$r_{\text{ISCO}}(\text{M})$	Inf. disk	Thin disk	Thick disk	Torus
0	6.000	625	1532	115	39
0.1	5.669	440	1282	92	31
0.2	5.329	301	1130	72	25
0.3	4.979	213	1348	55	19
0.4	4.614	143	1610	40	15
0.5	4.233	93	2796	29	11
0.6	3.829	58	537	19	8
0.7	3.393	34	46	10	5
0.8	2.907	18	19	5	3
0.9	2.321	7	8	3	2
0.92	2.180	5	6	2	2
0.94	2.024	4	5	2	1
0.96	1.843	3	4	1	1
0.98	1.614	2	3	1	1

Note. — The timescale t_{CB} required for the build-up of a magnetic field of $\mathcal{B}_o = 10^7$ G around a $5M_{\odot}$ black hole for various black hole spin parameters and accretion disk models.

sive part of the disk has been called the *Cosmic Battery* (Contopoulos & Kazanas 1998). Its physical significance is that, since only the plasma electrons feel the radiation force, they are the only ones that slow down or accelerate in the azimuthal direction, gradually building up a relative velocity between themselves and the protons. This is equivalent to an azimuthal electric current which gives rise to the poloidal magnetic field through the ISCO. In other words, the azimuthal radiation force works most efficiently (maximum radiation pressure, maximum plasma velocities, and maximum radiation-plasma motion misalignment) to grow astrophysically significant magnetic fields of order $\mathcal{B}_o \sim 10^7$ G (for stellar mass black holes) inside the ISCO over timescales roughly equal to

$$t_{\text{CB}} \sim \frac{e\mathcal{B}_o r_{\text{ISCO}}}{\alpha_{\text{ISCO}} f_{\text{rad}}^{\hat{\phi}} c}. \quad (29)$$

The latter estimate is obtained from dimensional analysis of eq. (27). The values of t_{CB} that correspond to $\mathcal{B}_o = 10^7$ G for a $5M_{\odot}$ black hole for various black hole spin parameters and for various accretion disk models are shown in Table 4. The characteristic timescales that we obtain vary from a few hours (in the case of maximally rotating black holes) to several days (in the case of slowly rotating ones). We do acknowledge here that we did not take into consideration the fact that as soon as the magnetic field approaches its equipartition value, magnetic stresses will begin to affect the plasma velocity field germane to its origin. Such stresses are proportional to the square of the magnetic field, thus, they are expected to become significant only when the magnetic field grows above about 30% of its equipartition value. Our growth timescales t_{CB} must, therefore, be taken as rough order of magnitude estimates.

notesize

5. CONCLUSIONS

Our analysis of the radiation field in the immediate vicinity of an accreting rotating black hole generalizes

the classical PR drag effect in new and unexpected ways. In the case of optically thick disks, the rotation of the disk and spacetime change the azimuthal force from drag to acceleration, while the drag is recovered in the case of infinitely thin disks. It is estimated that optically thin disks will also experience radiation drag, but this remains to be shown in future calculations. Moreover, the complex radiation field is expected to dramatically modify the dynamics of the disk around its inner edge. Not only that. The azimuthal component of the radiation force introduces an azimuthal electromotive source term in the induction equation which very naturally accounts for the generation of equipartition-level magnetic fields within astrophysically relevant timescales (hours to days in stellar mass black hole X-ray binaries). Note that our present realistic results differ significantly from previous estimates based on the classical PR drag effect obtained under the assumption of a central isotropic luminosity source (Contopoulos & Kazanas 1998, Kylafis *et al.* 2012).

We have just begun to investigate the astrophysical implications of the complex radiation field generated by the accretion disk in the vicinity of a rotating black hole. Our numerical setup is ideally suited to address several other important effects in future investigations:

1. The optical depth of the disk: Photons are emitted and absorbed from a certain depth below the surface of the disk. This effect is expected to be very important in optically thin geometrically thick accretion disks (e.g. ADAF), and in particular in situations where the type of the inner disk transitions from optically thin geometrically thick to optically thick geometrically thin, as is the case in the various stages in the q-diagram of flaring X-ray binaries (e.g. Belloni 2010). Consideration of the optical depth will yield a more realistic distribution of the azimuthal electromotive source of the Cosmic Battery mechanism.
2. A more realistic accretion disk velocity field where the assumptions that $v^r \ll v^\phi$ and $v(r, \theta) = v(r, \pi/2)$ in the disk are relaxed.
3. Retrograde disk rotation (our present results were obtained only for prograde Keplerian rotation).
4. More general temperature profiles.
5. The dynamics of the inner accretion flow: The radial radiation pressure will displace the inner edge of the disk. At the same time, the azimuthal radiation force is expected to dramatically modify the accretion flow. Both effects may be associated with the observed intense variability in X-ray binaries, disk instabilities, the q-diagram, etc. (Kylafis *et al.* 2012).

We conclude that the radiation field in the vicinity of an accreting astrophysical black hole modifies the accretion flow and generates complex electromagnetic dynamics that may be associated with the origin and evolution of magnetic fields and outflows in energetic astrophysical sources such as X-ray binaries and AGNs.

This work was supported by the General Secretariat for Research and Technology of Greece and the European Social Fund in the framework of Action ‘Excellence’.

notesize

APPENDIX A: PARTICLE TRAJECTORIES

In the study of particle trajectories in Classical Mechanics, we often use conserved quantities. In the same manner, when studying particle trajectories in Kerr spacetime it is not only useful, but unavoidable to seek and use the integrals of motion, most of which are already known from Classical Mechanics. A particle with four-momentum $p = (p^t, p^r, p^\theta, p^\phi)$ in geodesic motion around a rotating black hole has four conserved quantities: its rest mass m , its total energy $E = -p_t$, its angular momentum component parallel to the symmetry axis $L = p_\phi$, and the Carter constant $Q = p_\theta^2 + \cos^2 \theta [a^2(m^2 - p_t^2) + p_\phi^2 / \sin^2 \theta]$. The latter can be thought of as a measure of how much the trajectory deviates from the equatorial plane (a particle that starts from the equatorial plane with $Q = 0$ will remain there, whilst a particle that starts outside the equatorial plane with $Q > 0$, will eventually cross it at some point).

Particle trajectories satisfy the equations of motion (?)

$$\begin{aligned} \Sigma \frac{dr}{d\lambda} &= \pm (V_r)^{1/2} \\ \Sigma \frac{d\theta}{d\lambda} &= \pm (V_\theta)^{1/2} \\ \Sigma \frac{d\phi}{d\lambda} &= -(aE - L / \sin^2 \theta) + aT / \Delta \\ \Sigma \frac{dt}{d\lambda} &= -a(aE \sin^2 \theta - L) + (r^2 + a^2)T / \Delta \end{aligned} \quad (30)$$

where λ is an affine parameter along the trajectory ($\lambda = \tau/m$ for massive particles), and

$$\begin{aligned} T &\equiv E(r^2 + a^2) - La \\ V_r &\equiv T^2 - \Delta [mu^2 r^2 + (L - aE)^2 + Q] \\ V_\theta &\equiv Q - \cos^2 \theta [a^2(m^2 - E^2) + L^2 / \sin^2 \theta] . \end{aligned} \quad (31)$$

For a massive particle like an electron, we can set $m = 1$, and for a massless one like a photon, we take $m = 0$. Even though the above form of the equations of motion is compact and elegant, during numerical integration it proves to be highly problematic. The presence of the square roots of the potentials at the first two equations, accumulates errors rather quickly at the turning points. Also, in this form, one would have to change the signs of the square roots by hand at the turning points, something that causes the execution of even medium resolution codes to be almost impossible. There are various ways of dealing with the aforementioned problems. We have found it to be more convenient to transform the above four equations of motion into an equivalent Hamiltonian system of six equations (plus two conserved quantities) and integrate that instead. The new equations of motion are

$$\frac{dt}{d\lambda} = \frac{1}{2\Sigma\Delta} \frac{\partial}{\partial E} (V_r + \Delta V_\theta)$$

$$\begin{aligned}
 \frac{d\phi}{d\lambda} &= -\frac{1}{2\Sigma\Delta} \frac{\partial}{\partial L} (V_r + \Delta V_\theta) \\
 \frac{dr}{d\lambda} &= \frac{\Delta}{\Sigma} p_r \\
 \frac{d\theta}{d\lambda} &= \frac{1}{\Sigma} p_\theta \\
 \frac{dp_t}{d\lambda} &= 0 \\
 \frac{dp_\phi}{d\lambda} &= 0 \\
 \frac{dp_r}{d\lambda} &= -p_r^2 \frac{\partial}{\partial r} \left(\frac{\Delta}{2\Sigma} \right) - p_\theta^2 \frac{\partial}{\partial r} \left(\frac{1}{2\Sigma} \right) + \frac{\partial}{\partial r} \left(\frac{V_r + \Delta V_\theta}{2\Sigma\Delta} \right) \\
 \frac{dp_\theta}{d\lambda} &= -p_r^2 \frac{\partial}{\partial \theta} \left(\frac{\Delta}{2\Sigma} \right) - p_\theta^2 \frac{\partial}{\partial \theta} \left(\frac{1}{2\Sigma} \right) + \frac{\partial}{\partial \theta} \left(\frac{V_r + \Delta V_\theta}{2\Sigma\Delta} \right).
 \end{aligned}$$

These are the equations that code *Omega* solves numerically, backtracking the path followed by the photon that hit the target, until it finds its point of origin on the radiating disk.

Let us now address another subject that directly relates to the equations of motion. As we saw in eqs. (20) and (26), in order to calculate the Doppler shift and the flux in the LNRF at the position of the target, we need to know the source and target four-velocities. Since both are on the accretion disk, all we need to calculate is the disk four-velocity at different radii. Even though our disk models are in general ‘thick’ (i.e. they extend beyond the equatorial plane), in order to simplify the process of solution we assume that $v^\phi(r, \theta) = v^\phi(r, \pi/2)$. We also consider only cases with $v^r \ll v^\phi$, i.e. $v \approx v^\phi$. Solving now the equations of motion (30) for circular prograde equatorial orbits, the four-velocity components are

$$\begin{aligned}
 u_t &= -\frac{r^{3/2} - 2Mr^{1/2} + aM^{1/2}}{r^{3/4}(r^{3/2} - 3Mr^{1/2} + 2aM^{1/2})^{1/2}} \\
 u_\phi &= \frac{M^{1/2}(r^2 - 2aM^{1/2}r^{1/2} + a^2)}{r^{3/4}(r^{3/2} - 3Mr^{1/2} + 2aM^{1/2})^{1/2}} \quad (32)
 \end{aligned}$$

We define the quantity

$$\Omega = \frac{d\phi}{dt} = \frac{u^\phi}{u^t} = \frac{M^{1/2}}{r^{3/2} + aM^{1/2}}. \quad (33)$$

In order to calculate the velocity needed for the Doppler shift, simple calculations yield

$$v^{\hat{\phi}} = \frac{u^{\hat{\phi}}}{u^{\hat{t}}} = \frac{\varpi}{\alpha} (\Omega - \omega). \quad (34)$$

We can now rewrite eq. (22) explicitly for the frequency shift

$$\frac{\nu}{\nu_s} = \left(\frac{\Delta_s \Sigma_s / A_s}{\Delta \Sigma / A} \right)^{1/2} \frac{1 + \frac{2Mar}{A} \frac{p_\phi}{p_t}}{1 + \frac{2Mar_s}{A_s} \frac{p_\phi}{p_t}} \frac{[1 - (v^{\hat{\phi}})^2]^{1/2}}{1 - v^{\hat{\phi}} \cos \psi} \quad (35)$$

where the subscript s refers to quantities calculated at the radius of the source. The specific intensity perceived in the LNRF at the position of the target will hence be

$$I = \left(\frac{\Delta_s \Sigma_s / A_s}{\Delta \Sigma / A} \right)^2 \left(\frac{1 + \frac{2Mar}{A} \frac{p_\phi}{p_t}}{1 + \frac{2Mar_s}{A_s} \frac{p_\phi}{p_t}} \right)^4 \frac{[1 - (v^{\hat{\phi}})^2]^2}{(1 - v^{\hat{\phi}} \cos \psi)^4} I_s. \quad (36)$$

In future work, we intend to improve our results by numerically generating full maps that give the exact velocity and four-velocity components for every point of the disk. Although the results will be more accurate, we do not expect them to differ greatly from the ones presented in Table 1.

notesize

APPENDIX B: NUMERICAL CODES AND PHOTON TRAJECTORIES

In this section we describe the main important aspects of our two numerical codes, *Omega* and *Infinity*, and we list their specifications. We also show diagrams generated with code *Omega* that reveal the importance of the spacetime rotation and its impact on the ‘allowed photon trajectories’.

Code *Omega* is responsible for the ray tracing process and the graphical representation of the compact object, the accretion disk and the photon trajectories. The code draws the event horizon, the ergosphere, and the photon sphere. For each photon trajectory, it displays its length and end (at the target electron), along with a marker at the source whose color represents the type of point of origin. For the accretion disk, the inner, hotter part is drawn, along with the ISCO and the outer radius outside which we consider the disk to be cold and thus emitting negligible radiation. If the user desires so, an extension of the cold disk can be drawn for representation. Finally, for every trajectory the three constants of motion E , L and Q are shown along with the photon four-momentum product $p_\mu p^\mu$ at the beginning and the of the orbit (or any other intermediate point) in order to ensure that it is close to zero, as it should be for a photon. The code at the end returns and outputs the coordinates of the point of origin.

The interface of code *Omega* is user-friendly with buttons, sliders or input boxes that allow total command on any aspect of the problem. The controllable fields are

1. **The disk model:** The user can choose the shape of the disk from the following:

- (a) no accretion disk,
- (b) a zero-thickness band of radiation at the distance of the ISCO,
- (c) an infinitely thin disk at the equatorial plane,
- (d) a slab of equal thickness at all points with half-height h ,
- (e) a wedge-like accretion disk of equal angle at all points and a half-height h at the ISCO and
- (f) a torus whose generating circle has a radius r_{tor} and its inner edge lies on the ISCO.

2. **Cold disk:** The user can choose whether a part of the cold disk is visualized.

3. **The upper limit for the affine parameter λ :** The trajectory integration normally stops at an arbitrary radius of $12M$ but the user can choose to stop it at any point before or after that, as long as no point of origin is found.

4. **The spin parameter:** The dimensionless spin parameter $j = a/M$ is set.
5. **The target electron position:** By default, the target electron is set at the equatorial plane ($\theta = \pi/2$) at the distance of the ISCO ($r = r_{ISCO}$). It is possible though for the user to input initial positions of his/her own choice.
6. **The band half-height:** The user can control the height of the disk at the distance of the ISCO for the models that have the corresponding dimension.
7. **The angles of photon incidence:** The angles \hat{a} and \hat{b} of the incoming photon can be input by the user with any accuracy. The former takes values from 0° to 180° and the latter from 0° to 360° . If the user however desires to enter different values, this is also possible.
8. **The zoom:** The user can zoom in or out of the picture in order to view the result with more detail or to see the bigger picture. The output 3D image of the disk and the photon trajectory can also be rotated in any direction to allow better viewing for the various trajectories.

Code *Infinity* first separates the sky of the target particle into a grid. Then, it uses code *Omega* as a subroutine and scans across that grid in order to calculate the frequency integrated specific intensity at each point. The various shifts for each trajectory are calculated by separate subroutines. After the radiation matrices are created, the code calculates the stress-energy tensor in the LNRF using eq. (16). Then it calculates the radiation pressure force through eqs. (12) or (26), depending on the user's choice of reference frame. The interface of code *Infinity* is also user-friendly and compact. It is composed of seven popup menus that allow the user to fully specify the parameters of the problem. These fields are

1. **The disk model:** Similar to code *Omega*. The user can choose between the band, the thin disk, the slab, the wedge and the torus.
2. **The disk temperature model:** The user chooses between an isothermal disk with $T(r_s) = \text{const.}$, or an accretion disk with $T(r_s) \propto r_s^{-3/4}$.
3. **Grid size:** The resolution of the target's sky grid is set by the user. Although in our study we work with a $0.5^\circ \times 0.5^\circ$ grid, depending on the the time and accuracy needs, one can choose from a variety of grid sizes ranging from $10^\circ \times 10^\circ$ all the way down to $0.25^\circ \times 0.25^\circ$.
4. **Disk half-height:** Similar to code *Omega*. It controls the height of the disk at the distance of the ISCO for the band, the slab, the wedge and the torus models.
5. **Black hole mass:** The central black hole mass can be chosen from a list ranging from $1M_\odot$ up to $4.5 \times 10^6 M_\odot$ (the estimated mass for a Milky Way-size supermassive black hole).
6. **Spin parameter:** The spin parameter a of the black hole can be chosen from a list of more than 20 values from 0 to $0.999M$.
7. **Reference frame:** Simulation results can be expressed either in the LNRF or the Boyer-Lindquist frame at the position of the target.

Finally, in Figure 5 we present representative photon trajectories as obtained using code *Omega* in order to elucidate the main effects introduced by the spacetime rotation. The images depict the system as seen from above the equatorial plane. The changes in the orbits are easily noticeable as the black hole spin increases.

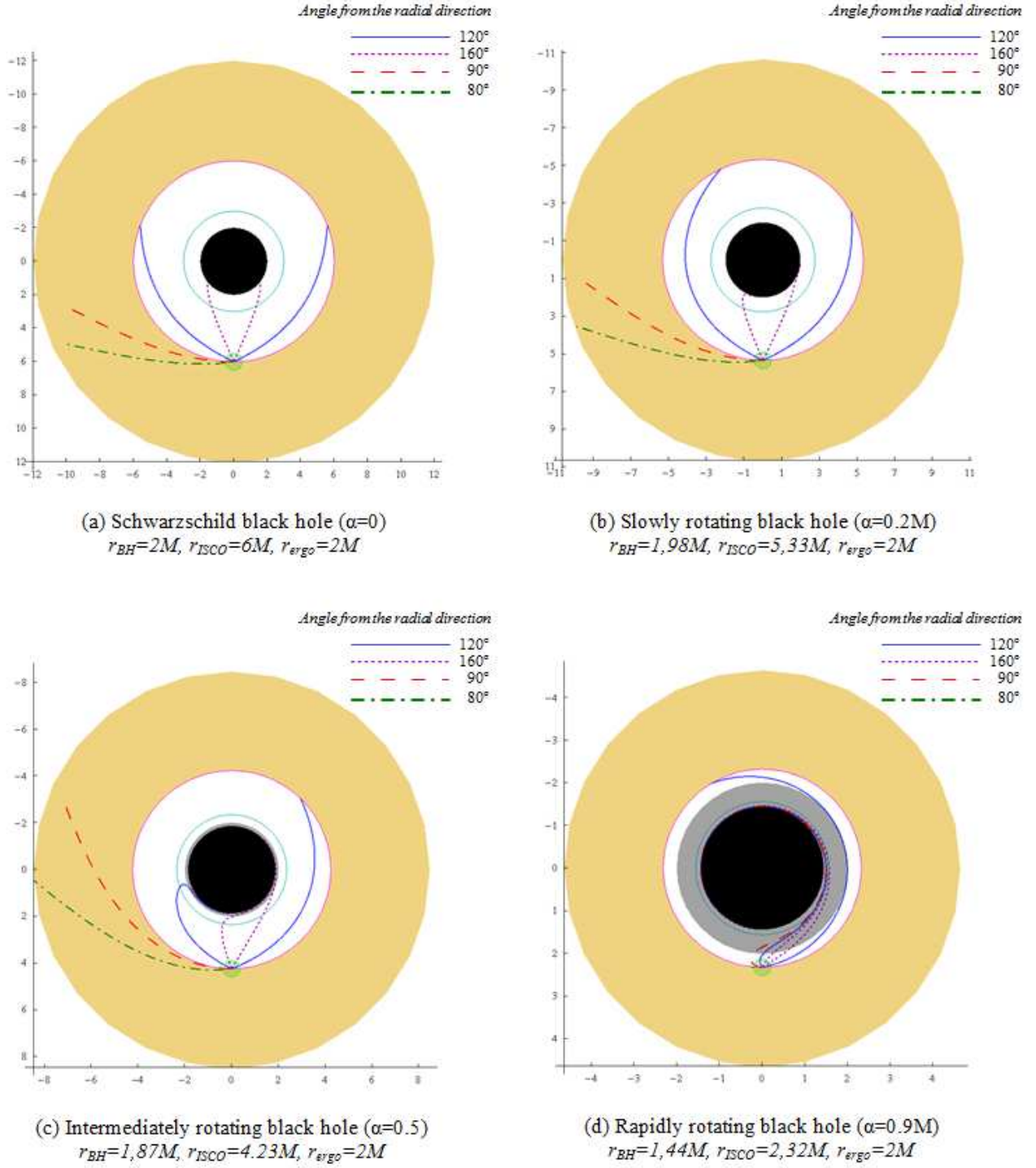


Figure 5. The equatorial plane and photon trajectories around clockwise rotating black holes of different spin parameters. The black disk is the event horizon, the grey annulus is the ergosphere, the inner circle is the photon sphere, the outer is the ISCO and the shaded area outside it, is the rest of the accretion disk. The trajectory angles are measured from the (outward) radial direction and the accretion disk rotates clockwise. Notice that as a increases, we zoom into the picture in order to better see the details. The effects of the rotation on the photon trajectories are clearly visible as the spin parameter increases. The allowed photon trajectories tend to concentrate in the direction of motion.